

Investigation of the Role of Droplet Transport in Mitigating Top of the Line Corrosion

Nicolas Jauseau,^{‡,***} Fernando Farelas,^{*} Marc Singer,^{*} and Srdjan Nešić^{*}

ABSTRACT

The entrainment of liquid droplets, occurring in a limited range of gas and liquid flow conditions within the stratified flow region, could represent an effective way to transport a non-volatile liquid corrosion inhibitor through the gas phase and combat top of the line corrosion (TLC). However, such an approach is only viable if the inhibitor can reach the top of the pipe and deposit at a rate higher than the local rate of condensing water can dilute it. This work presents a combined modeling and experimental methodology to determine the onset of droplet entrainment from the bottom and deposition at the top of the line. A modeling approach predicting the droplet entrainment onset is proposed and validated against new multiphase flow data recorded in a large scale flow loop, at operating conditions similar to those encountered in gas-condensate production facilities. Additionally, TLC experiments were performed in the same flow loop under simulated water condensation conditions to measure the actual corrosion at different rates of inhibiting droplet deposition. The results confirm that the droplet entrainment/deposition can effectively mitigate TLC when operating parameters are accurately controlled.

KEY WORDS: droplet deposition, droplet entrainment, inhibition, top of the line corrosion

Submitted for publication: January 17, 2018. Revised and accepted: March 28, 2018. Preprint available online: March 28, 2018.
<https://doi.org/10.5006/2764>.

[‡] Corresponding author. E-mail: nicolas.jauseau@kdi.kongsberg.com.

^{*} Institute for Corrosion and Multiphase Technology, Ohio University, 342 West State St, Athens, OH 45701.

^{**} Present address: Kongsberg Digital Inc., 10777 Westheimer Rd, Suite 1200, Houston, TX 77042.

INTRODUCTION

Top of the line corrosion (TLC) is a major challenge for many oil and gas operators because it causes pipe failures.¹⁻⁶ It occurs in stratified flow regime in horizontal and near-horizontal pipelines under water condensing conditions. Continuous injection of standard chemical inhibitors is often used to mitigate TLC in production pipelines, but this method is only effective when the continuous liquid phase remains in contact with the pipe wall. Consequently, TLC mitigation remains a serious challenge as there is no straightforward way to transport the inhibitor present in the continuous liquid phase flowing at the bottom of the pipe to the top of the line. The use of concentrated inhibitor periodic batch treatments and deployment of volatile corrosion inhibitors are some of the currently proposed solutions, but they also present many technical challenges, such as: selection of the proper volatile inhibitor package, verification of its effectiveness under TLC conditions, persistency of protection in batch treatment, selection of optimum batch frequency, etc.⁷⁻⁹

A change in the flow regime from stratified to non-stratified (e.g., annular or slug flow) could aid the continuous liquid phase to reach the top of the pipe and, thus, mitigate the problem, but may not be desirable from a flow assurance standpoint (i.e., mechanical stress on pipelines, separation issues at arrival facilities, erosion, etc.). However, inhibition may also be achieved in stratified flow when droplet entrainment is considered. At sufficiently high gas velocity, liquid droplets containing inhibitor can be

sheared off from the bulk liquid phase at the bottom of the line and transported to the top via the gas phase. Once deposited at the top of the pipe, the inhibitor will still have to “compete” with the condensation of fresh water, which otherwise would dilute it and diminish its efficiency. Although this mitigation approach has been identified by several researchers,¹⁰⁻¹¹ to the best of the authors’ knowledge, it has never been properly evaluated in a laboratory setting or in a field environment.

Operating conditions in gas-condensate pipelines, usually 14 in to 40 in (0.356 m to 1.016 m) inner pipe diameter, feature medium to high pressures, where a gas phase characterized by high fluid densities ($\geq 60 \text{ kg/m}^3$) flows at relatively low gas velocities (5 m/s to 15 m/s). Because of the complexity, cost, and hazards, such field conditions are difficult to reproduce in a laboratory facility. On the other hand, droplet transport models that can be found in the literature are based on laboratory data collected at much higher gas velocities (15 m/s to 100 m/s) in low-pressure environments ($<0.5 \text{ MPa}$ total pressure), which produce equivalent interface forces,¹² proportional to gas density and velocity: $\rho_G U_G^2$. These large differences in gas velocity between the lab and field conditions affect not only the appearance and behavior of the stratified liquid/gas interface at the bottom of the line, but also the nature of dropwise condensation at the top, which makes the direct application of such lab results to the field difficult.

The present study addresses some of these limitations, by investigating the influence of droplet transport on carbon dioxide (CO_2) driven TLC.

A model is developed to determine the onset of droplet entrainment and deposition at the top of the line. The modeling approach is supported by an experimental study performed in a large scale flow loop, focusing on the measurement of droplet entrainment and by using a heavy molecular weight gas to simulate high gas density seen in the field. A second experimental study, dedicated to TLC in water condensing conditions, is also performed to verify the overall approach.

DEVELOPMENT AND VALIDATION OF THE DROPLET TRANSPORT MODEL

Modeling of Entrainment Onset

Mechanisms of Entrainment Onset — The entrainment of liquid droplets in a gas phase can be initiated by different mechanisms, such as: wave entrainment (Figure 1), bubble burst entrainment, and droplet impingement entrainment (Figure 2). The wave entrainment is the dominant entrainment mechanism in the present applications, with the other two being of secondary importance.¹³⁻¹⁷ In the case of wave entrainment, the droplets are formed from disturbance waves (3D roll waves) created at the gas/liquid interface.

Wave entrainment can take various forms, such as wave coalescence, wave undercutting, and ripple wave shearing-off (Figure 1).¹³ Among those, the ripple wave shearing-off, during which a wavelet at the wave crest is torn away and generates liquid droplets, is considered the dominant one.¹⁶ At very low liquid loadings (low liquid Reynolds numbers, Re_L), this wave entrainment mechanism does not occur. However, liquid droplets can still be formed by wave undercutting at sufficiently high

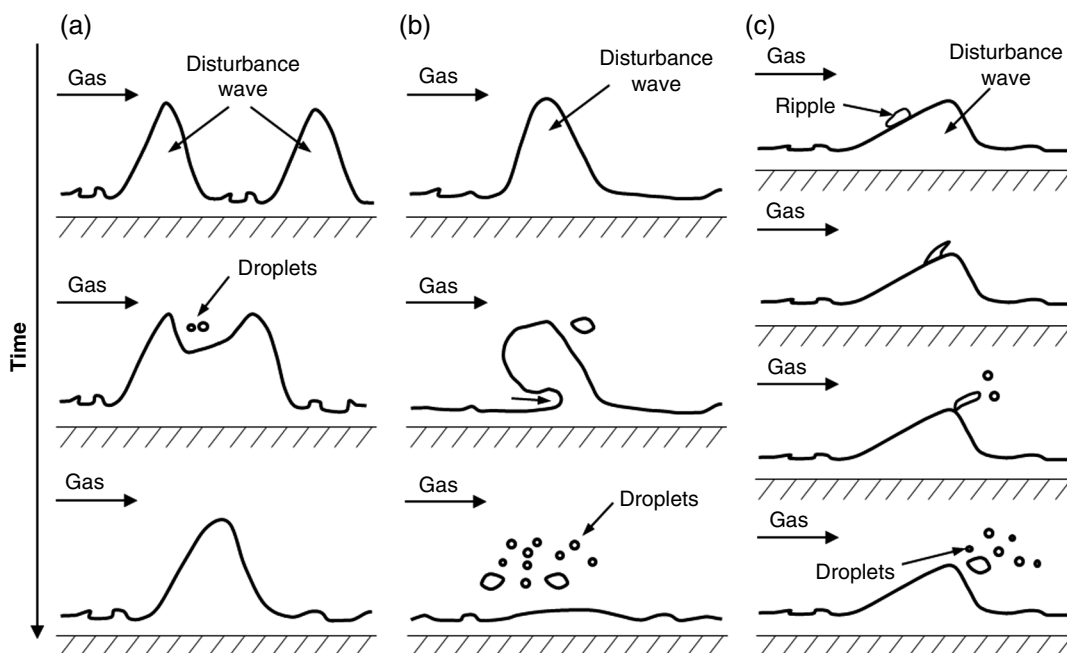


FIGURE 1. Mechanisms of droplets formation by wave entrainment: (a) wave coalescence, (b) wave undercutting, and (c) ripple wave shearing-off (adapted from Han and Gabriel¹³).

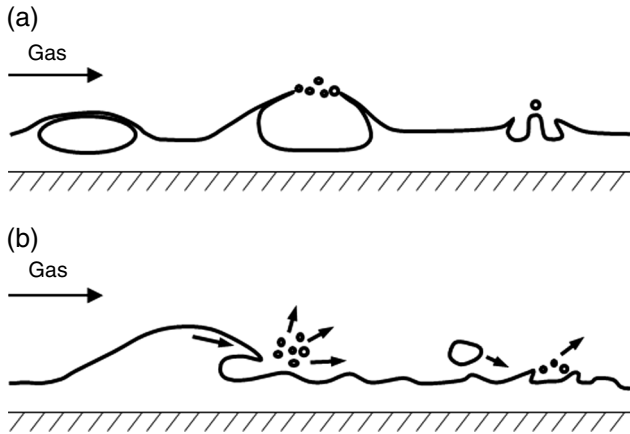


FIGURE 2. Secondary mechanisms of droplets formation: (a) bubble burst and (b) droplet impingement at the gas/liquid interface (adapted from Ishii and Grolmes¹⁴).

gas velocities. In this case, a disturbance wave can be sheared-off into the gas core, and then, disintegrated into smaller liquid droplets.¹³⁻¹⁴ Additionally, wave undercutting can occur at higher liquid flow rates in viscous fluids.¹⁵ Therefore, to model the entrainment onset, the present study considers both forms, the ripple wave shearing-off and wave undercutting.

Definition of the Entrainment Onset — The occurrence of the entrainment onset is considered when some liquid droplets are torn from the gas/liquid interface, i.e., when the atomization of liquid droplets occurs. In order to consider entrainment onset significant in horizontal pipe, one requires that the droplets are able to impinge on the top of the pipe. This is particularly important because it also defines the deposition of the liquid droplets in TLC, which has been observed previously in wet gas pipelines. The entrainment onset mechanism can be separated in three distinct regions. Below a critical liquid Reynolds number (low liquid flow rate), the superficial gas velocity required to initiate the droplet entrainment sharply increases reaching the entrainment limit.¹⁸ At high liquid flow rates, no entrainment onset occurs below a critical gas velocity. Between these two limiting cases, the inception of droplet entrainment depends on both liquid and gas flow rates.

Model Description — The modeling of entrainment onset transition follows the approach initially developed by Ishii and Grolmes, and later completed by Mantilla and coworkers.¹⁹ Briefly, a force balance (Figure 3) is applied to a single wave, and consists of the drag force, F_D , the surface tension force, F_σ , and the gravitational force, F_g :

$$F_D \geq F_\sigma + F_g \sin(\beta) \quad (1)$$

The drag force is defined as:

$$F_D = \frac{1}{2} C_D \lambda_w \Delta h_w \rho_G (U_G - U_L)^2 \quad (2)$$

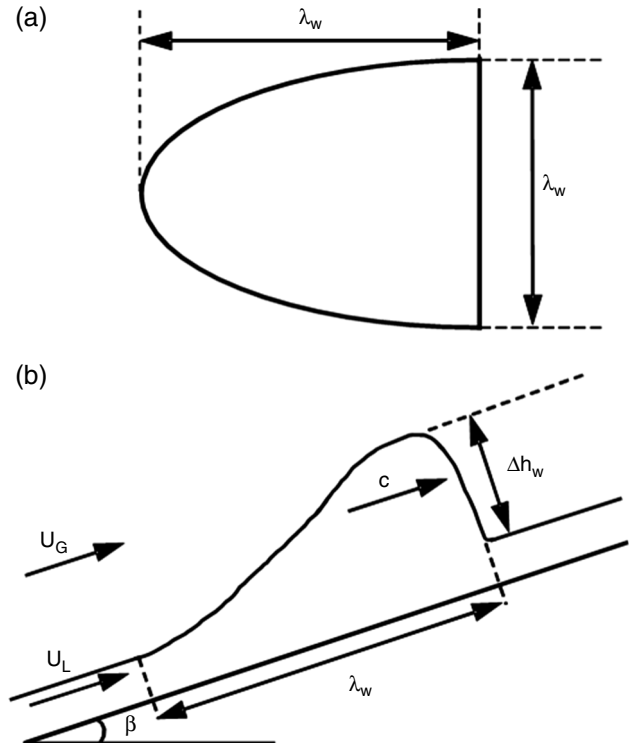


FIGURE 3. (a) Top view and (b) side view of a wave (adapted from Mantilla²⁴).

C_D is the drag coefficient taken as $C_D = 0.95$ for irregular shapes. λ_w and Δh_w represent the length and height of the liquid wave, respectively.

The surface tension force is given by:

$$F_\sigma = C_S \lambda_w \sigma \quad (3)$$

C_S is the interfacial shape coefficient taken as $C_S = 0.77$ and corresponds to the average wave crest with a half-elliptic base.¹⁴

The gravity force is calculated as:

$$F_g = \frac{\pi}{8} \lambda_w^2 \Delta h_w \rho_L g \sin(\beta) \quad (4)$$

By substituting Equations (2) through (4) into Equation (1), it yields:

$$C_D \Delta h_w \rho_G (U_G - U_L)^2 = 2 C_S \sigma + \frac{\pi}{4} \lambda_w \Delta h_w \rho_L g \sin(\beta) \quad (5)$$

Following Ishii and Grolmes' recommendations, the interfacial shear stress at the wave crest τ_i is assumed to be proportional to the liquid film velocity:

$$\tau_i = C_w \mu_L \frac{U_L}{\Delta h_w} \quad (6)$$

C_w represents the effect of surface tension forces on the internal flow within the wave crest and can be

expressed as a function of the liquid viscosity number N_μ , such as:

$$\frac{1}{3C_w} = \begin{cases} 11.78N_\mu^{0.8}, & N_\mu \leq \frac{1}{15} \\ 1.35, & N_\mu > \frac{1}{15} \end{cases} \quad (7)$$

where

$$N_\mu = \mu_L \times \left[\rho_L \sigma \sqrt{\frac{\sigma}{(\rho_L - \rho_G)g}} \right]^{-1/2} \quad (8)$$

The interfacial shear stress τ_i can be calculated using either the liquid- or gas-interfacial friction factor, such as:

$$\tau_{Gi} = f_{Gi} \frac{\rho_G (U_G - U_L)^2}{2} \quad (9)$$

$$\tau_{Li} = f_{Li} \frac{\rho_L U_L^2}{2} \quad (10)$$

Using Hughmark,²⁰ the liquid-interfacial friction factor τ_{Li} is defined as:

$$f_{Li} = \sqrt{1.962/Re_L^{1/3}} \quad (11)$$

where

$$Re_L = \frac{\rho_L D_L U_L}{\mu_L} \quad (12)$$

The gas-interfacial friction factor f_{Gi} was initially expressed as a constant. Mantilla¹⁹ accounted for the effect of pipe diameter because the friction factor is related to the relative roughness of the wave amplitude. A new correlation was developed and tuned with the help of a subset of randomly sampled experimental data collected in the present study for different gas-liquid mixtures of CO₂/water and sulfur hexafluoride (SF₆)-CO₂/water.²¹ This subset of experimental data was not included in the set used for the validation of the model. The expression of f_{Gi} is shown below:

$$f_{Gi} = C_0 \left(\frac{T}{T^0} \right)^{C_1} \left(\frac{P}{P^0} \right)^{C_2} \left(\frac{MW_G}{MW_{air}} \right)^{C_3} \left(\frac{h_L}{D} \right)^{C_4} \quad (13)$$

where $C_0 = 0.00140820$, $C_1 = -3.41122637$, $C_2 = 0.40052095$, $C_3 = 0.33121546$, and $C_4 = -0.23537017$. MW_G and MW_{air} are the molecular weights of the gas phase and air, respectively ($MW_{air} = 28.97$ g/mol). Temperatures are expressed in degree Kelvin.

Assuming that $\tau_i = \tau_{Li}$ and using the shear stress continuity at the interface $\tau_{Li} = \tau_{Gi}$, substituting Equations (9) and (10) into Equation (6) yields the following expression:

$$\Delta h_w = 2C_w \frac{\mu_L}{\rho_L} \sqrt{\frac{\rho_L}{\rho_G} \times \frac{1}{f_{Li} f_{Gi}}} \frac{1}{U_G - U_L} = \frac{C_r}{U_G - U_L} \quad (14)$$

where

$$C_r = 2C_w \frac{\mu_L}{\rho_L} \sqrt{\frac{\rho_L}{\rho_G} \times \frac{1}{f_{Li} f_{Gi}}} \quad (15)$$

Substituting Equation (14) into the force balance Equation (5) gives the following expression:

$$(U_G - U_L)^2 - 2 \frac{C_S \sigma}{C_r C_D \rho_G} (U_G - U_L) - \frac{\pi \lambda_w \rho_L g \sin(\beta)}{4 C_D \rho_G} \quad (16)$$

This second degree polynomial has two possible solutions. The negative solution is discarded, while the positive solution represents the entrainment onset criterion:

$$U_G - U_L = \frac{C_S \sigma}{C_r C_D \rho_G} + \sqrt{\left(\frac{C_S \sigma}{C_r C_D \rho_G} \right)^2 + \frac{\pi \lambda_w \rho_L g \sin(\beta)}{4 C_D \rho_G}} \quad (17)$$

The liquid velocity is taken as being the wave celerity c , which can be expressed as a function of the pipe inclination:²²

$$c/U_{SL} = \begin{cases} 2.379X^{*-0.9}, & \beta = 0^\circ \\ 2.323X^{*-0.94}, & 10^\circ \leq \beta \leq 20^\circ \\ 1.942X^{*-0.91}, & \beta \geq 45^\circ \end{cases} \quad (18)$$

X^* is defined as the Froude numbers ratio between the liquid and gas phases:

$$X^* = \frac{Fr_{SL}}{Fr_{SG}} \quad (19)$$

$$Fr_{SL} = \sqrt{\frac{\rho_L U_{SL}^2}{(\rho_L - \rho_G)gD \cos \beta}} \quad (20)$$

$$Fr_{SG} = \sqrt{\frac{\rho_G U_{SG}^2}{(\rho_L - \rho_G)gD \cos \beta}} \quad (21)$$

The wave base length λ_w is expressed with the wave spacing L_w :

$$\lambda_w = L_w/2, \quad (22)$$

while the wave spacing is defined as:

$$L_w = 2\pi\sigma^{1/2} \left[\frac{(U_G - U_L)^2}{\frac{L_G}{\rho_G} + \frac{L_L}{\rho_L}} - (\rho_L - \rho_G)g \cos(\beta) \right]^{-1/2} \quad (23)$$

Both L_G and L_L are geometrical properties used in stratified flow and can be written as:

$$L_G = \frac{A_G}{dA_G/dh_G} \quad (24)$$

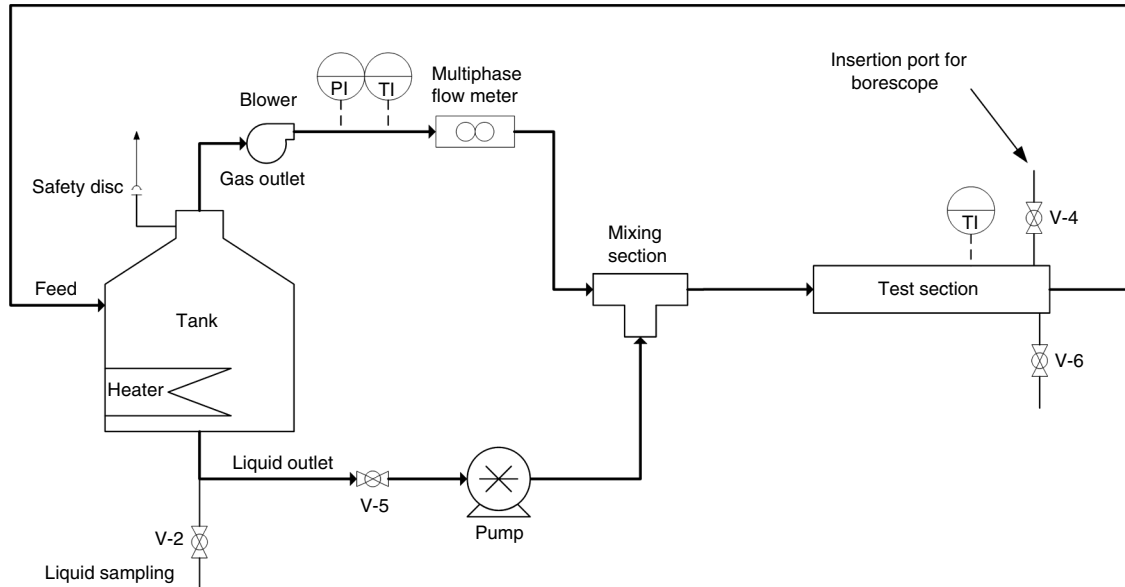


FIGURE 4. Process and flow diagram of the wet gas flow loop (experimental droplet transport).

$$L_L = \frac{A_L}{dA_L/dh_L} \quad (25)$$

Limiting Cases — At low liquid Reynolds numbers, the roll waves start disappearing as a result of a lower interfacial shear stress and a sudden increase in the critical velocity necessary to entrain the droplets.¹⁴ For low viscosity fluids, this transition occurs at a critical liquid film Reynolds number $Re_{L,crit}$, which varies with the flow inclination in pipe:

$$Re_{L,crit} = 2 \quad \text{if } \beta = -90^\circ \quad (26)$$

$$Re_{L,crit} = 160 \quad \text{if } \beta = 0^\circ \quad \text{or} \quad \beta = +90^\circ \quad (27)$$

Below $Re_{L,crit}$, the ripple wave shearing off mechanism does not occur. However, liquid droplets can still be formed by the wave undercutting mechanism when the liquid film Weber number We_L is in the range 17 to 22. The wave undercutting mechanism can be described by the following criterion using a Weber number of 22:

$$U_G - c = 1.5 \frac{\sigma}{\mu_L} \sqrt{\frac{\rho_L}{\rho_G} \times \frac{1}{Re_L}} \quad (28)$$

At high liquid Reynolds numbers ($Re_L > 5,000$), the friction factor is assumed to remain constant; therefore, a value of $Re_L = 5,000$ is used in Equation (11).

Experimental Study of Droplet Transport

Entrainment onset data found in the literature are scarce and often measured at operating conditions that are not representative for gas-condensate transportation pipelines (low gas density, high gas velocity). Therefore, an experimental setup was developed in this study to generate data as close as possible to the conditions observed in field operations. The experimental study involved a measurement of the droplet transport using visual observations at the transparent wall of the pipe (non-intrusive) and by using a borescope (camera) inserted within the pipe (intrusive).

Equipment — The experimental work was performed in a large scale wet gas flow loop, which was designed to study both droplet transport and CO₂ corrosion under two-phase gas-liquid flow conditions (Figure 4). The apparatus is a 4 in (0.102 m) pipe diameter 30 m long flow loop entirely made of UNS S31600⁽¹⁾ stainless steel, except for the test section; for droplet transport experiments, the latter consisted of a 5 m long transparent acrylic 4 in (0.102 m) pipe to visualize and record the flow regime occurring in the loop.

The gas phase could be either pure CO₂ or a CO₂/SF₆ mixture. The inert gas SF₆, characterized by a high molecular weight, was used to artificially increase the density of the gas stream in order to closely mimic conditions existing in pressurized gas production facilities. The gas flow rate, supplied by a gas blower, had a maximum capacity of 190.7 SCFM (0.09 Sm³/s) and was measured using a 5 psi (34.4 kPa) differential pressure transducer installed around a vortex flow meter. Deionized (DI) water was used as the liquid phase whose flow rate was controlled by a gear pump, which could deliver up to 9.5 gal/min (0.6×10^{-3} m³/s).

⁽¹⁾ UNS numbers are listed in *Metals and Alloys in the Unified Numbering System*, published by the Society of Automotive Engineers (SAE International) and cosponsored by ASTM International.

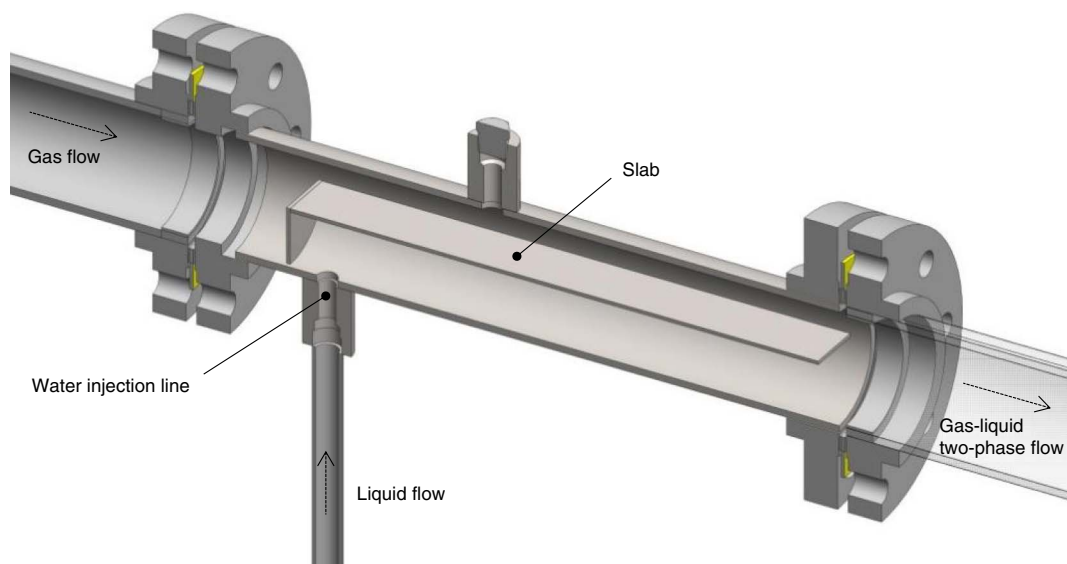


FIGURE 5. Cross-sectional view of the gas-liquid mixing section.

A slab was introduced at the mixing location between the gas and liquid phases to generate a fully segregated flow while minimizing liquid splashing (Figure 5); it should be noted that the intrusive slab did not generate a significant pressure drop in the flow loop. The test section was located at 60 L/D downstream of the mixing section. The instrumentation included pressure and temperature measurement devices, and a high-pressure borescope mounted on the pipe to record the onset of droplet entrainment. The borescope tip was positioned as close as possible to the top of the pipe, so that the droplet entrainment could be directly observed when droplets hit the lens of the borescope.

Methodology — The criterion to determine the onset of droplet entrainment in the pipe was that at least one liquid droplet should hit the borescope lens every 10 s. In such conditions and by considering the size of the droplets and the number of “hits” per surface area and per time, the corresponding deposition rate at the top of the line was roughly estimated to 0.001 mL/m²/s to 0.01 mL/m²/s.

Prior to the experiments, 300 L of DI water were introduced in the tank and sparged with CO₂ for 4 h to remove most of the O₂ and N₂ from the system. The composition of the gas stream was maintained constant by monitoring the partial pressure of each gas (i.e., CO₂ and SF₆) and was carefully recorded, as an increase in SF₆ concentration in the gas stream increased the gas density. Then, the borescope was introduced in the test section; the insertion port was carefully sealed to avoid any gas leak. During each experiment, the liquid flow rate was set to a constant value, whereas the gas flow rate was slowly increased until the droplet entrainment onset was achieved. Between each gas rate increment, a sufficient amount of time (usually 15 min

TABLE 1

Test Matrix for Droplet Transport Experiments

Parameters	Conditions
Gas phase	SF ₆ /CO ₂ (SF ₆ concentration in gas stream: 0 to 72 mol%)
Liquid phase	DI water
Superficial gas velocity (m/s)	5 to 12
Superficial liquid velocity (m/s)	0.004 to 0.072
CH ₄ equivalent pressure (MPa)	0.44 to 3.50
Temperature (°C)	25 to 40

to 30 min) was dispensed to make sure the flow loop truly reached steady-state conditions. Once the entrainment onset was observed on the borescope, the partial pressures, temperatures, and flow rates were recorded.

Using a constant gas composition, twenty independent series of measurements were performed by varying the superficial liquid velocity from 0.004 m/s to 0.072 m/s (see experimental conditions in Table 1). Using SF₆ instead of methane as a gas phase meant that only 0.5 MPa of SF₆ gas could approximate the same density as 5 MPa of methane as a result of the molecular weight difference (MW_{SF₆} = 146 g/mol vs. MW_{CH₄} = 16 g/mol). For consistency, the results are displayed as a function of the methane equivalent pressure $P_{CH_4}^{eq}$ (also noted eq P_{CH_4}) in the rest of the text.

Results — The experimental results in Figure 6 present a subset of the entrainment onset data collected in this study, expressing the critical superficial gas velocity $U_{SG,crit}$ above which droplets start to deposit at the top of the line as a function of the equivalent CH₄ pressure. At the lowest tested pressure ($P_{CH_4}^{eq} = 0.47$ MPa), the onset of droplet entrainment

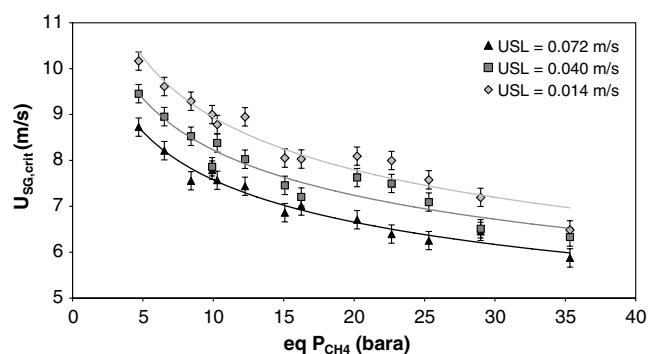


FIGURE 6. Droplet entrainment onset velocity at the top of the pipe as a function of total pressure and superficial liquid velocity U_{SL} .

was reached around $U_{SG,crit} = 10.3 \pm 0.2$ m/s at low liquid flow rate ($U_{SL} = 0.014$ m/s) and $U_{SG,crit} = 8.8 \pm 0.2$ m/s at higher liquid flow rate ($U_{SL} = 0.072$ m/s). As the liquid flow rate increases, the liquid holdup increases in the pipe and decreases the distance between the top of the pipe and the gas/liquid interface (a horizontal gas/liquid interface was reasonably assumed here). In turn, the cross-sectional area of the gas phase decreases and the in situ gas velocity slightly increases, allowing the droplet entrainment onset to occur at a lower gas velocity. As the total pressure (i.e., the gas density) increases, the interfacial shear stress between the gas and the liquid phase increases as well. Ripples and waves present at the gas/liquid interface can be further torn away to generate droplets. In a 4 in (0.102 m) pipe, the onset of droplet entrainment was observed for superficial gas velocities in the range of 6 m/s to 11 m/s at equivalent CH_4 pressure ranging from 0.4 MPa to 3.5 MPa. The entire collection of entrainment onset data is presented in Appendix A as a function of the mole fraction of SF_6 present in the gas phase, the superficial gas, and liquid velocities.

Entrainment Model Validation

The performance and accuracy of the droplet transport model were evaluated using statistical tools (Table 2), such as the average percent error, ϵ_1 , average absolute percent error, ϵ_2 , and percent standard deviation, ϵ_3 . These parameters require the determination of relative error, e_R , representing the deviation of predicted value (X_{pred}) from the experimental observation (X_{exp}).

A total of 258 entrainment onset measurements were collected in this study using different gas phase SF_6/CO_2 compositions. Additionally, entrainment onset data from literature²³⁻²⁴ were included in the database (Table 3); these additional data were measured at near-atmospheric pressure, featuring much higher gas velocities and lower gas densities compared to the present study. Overall, the entrainment onset database totaled 303 measurements. A random subsample of 33 data points was used for tuning the

TABLE 2

Statistical Tools Used for the Model Validation

Statistical Variable	Equation
Relative error	$e_R = \frac{X_{pred} - X_{exp}}{X_{exp}}$
Average percent error	$\epsilon_1 = \frac{1}{n} \left(\sum_{i=1}^n e_{R,i} \times 100 \right)$
Average absolute percent error	$\epsilon_2 = \frac{1}{n} \left(\sum_{i=1}^n e_{R,i} \times 100 \right)$
Percent standard deviation	$\epsilon_3 = \sqrt{\sum_{i=1}^n \frac{(e_{R,i} \times 100 - \epsilon_1)^2}{n-1}}$

TABLE 3

Experimental Data Used for the Entrainment Onset Model Validation

Authors	Data Points	Fluids	Pipe Diameter (m)
Andritsos ²³	14	Air/Water	0.025, 0.095
Andritsos ²³	10	Air/Water-Glycerine	0.025, 0.095
Mantilla ²⁴	14	Air/Water	0.049, 0.152
Mantilla ²⁴	4	Air/Water-Glycerine	0.049
Mantilla ²⁴	3	Air/Water-Butanol	0.049
This study	97	CO_2 /Water	0.095
This study	161	SF_6-CO_2 /Water	0.095

model; this subsample was not included in the model validation. Therefore, 270 measurements were finally used for model validation (Table 3). Based on statistical analysis tools (Table 2), the relative errors of the model predictions were calculated as the difference between the predicted and experimental superficial gas velocity at a given superficial liquid velocity, then averaged for each dataset and the entire database (Table 4). The model predicted most accurately the present study's data (2.9%), with consistent prediction errors (3.8%) regardless of the gas phase composition. A comparison between the predicted and measured entrainment onset is shown on a flow regime map (Figure 7), using two different gas compositions in the gas-liquid mixtures (pure CO_2 and mixture CO_2/SF_6).

A similar comparison was made for superficial gas velocity at the entrainment onset at different gas-liquid mixtures (Figure 8). The majority of data points fall within the $\pm 20\%$ deviations from the ideal agreement. The model agrees better with the entrainment onset observed with the borescope camera (present work and Mantilla) compared to the

TABLE 4

Performance Evaluation of the Entrainment Onset Model

Reference	Data Points	Statistics		
		ϵ_1 (%)	ϵ_2 (%)	ϵ_3 (%)
This study	225	+0.2	+2.9	+3.8
Andritsos ²³	24	-9.9	+26.7	+32.6
Mantilla, et al. ¹⁹	21	+10.9	+22.9	+28.4
All data	270	+0.1	+6.6	+13.4

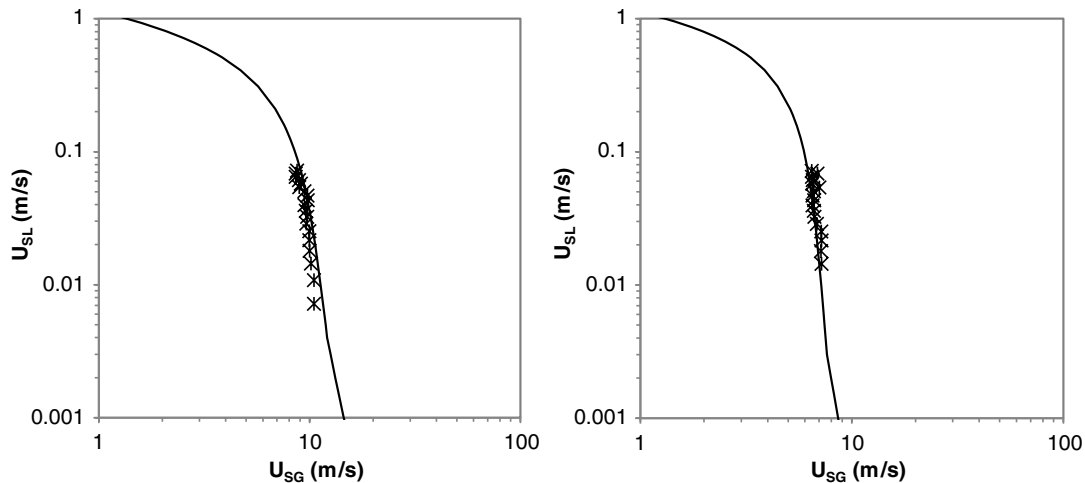


FIGURE 7. Predicted (line) vs. measured (markers) entrainment onset gas velocities for CO_2 -water mixture ($P_{\text{CH}_4}^{\text{eq}} = 0.47$ bara MPa, $T = 27.4^\circ\text{C}$) (left) and CO_2/SF_6 -water mixture with 72 mol% SF_6 ($P_{\text{CH}_4}^{\text{eq}} = 3.53$ bara MPa, $T = 29.3^\circ\text{C}$) (right).

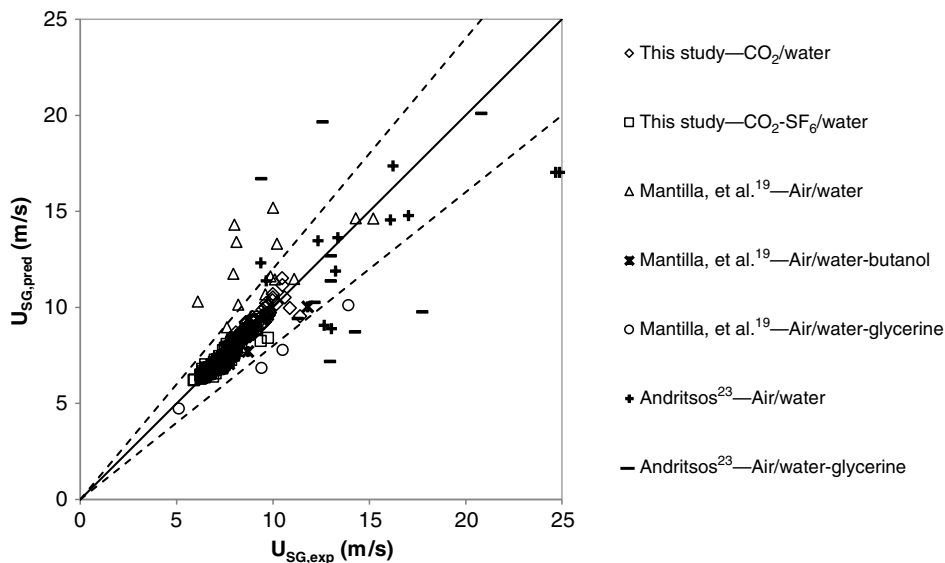


FIGURE 8. Predicted vs. experimental entrainment onset expressed as superficial gas velocity U_{SG} . Dashed lines represent the $\pm 20\%$ deviations from the 1:1 line.

entrainment onset detected visually, from outside the pipe.²³

Comparisons between the model and Mantilla data exhibited a slight overprediction (+10.9%) and an average absolute percent error of 22.9%. Unlike the entrainment onset criterion used in this study (see methodology), Mantilla's entrainment onset was defined as "a droplet hitting the top of the pipe every 5 to 10 seconds."²⁴ This difference in experimental data between the two studies may explain the overprediction of the droplet entrainment onset when considering air-water measurements (Figure 8). The large scattering observed with viscous fluid data (liquid phase as

water-glycerine) suggests that the present model does not account for the effect of viscosity very well; for more accurate entrainment onset predictions, only measurements from fluids with liquid viscosities less than 5×10^{-3} Pa·s should be used to validate this model.

INHIBITION OF THE TOP OF THE LINE CORROSION BY DROPLET TRANSPORT

A set of corrosion experiments was performed under high-pressure and high-temperature conditions in the large scale wet gas flow loop to validate the

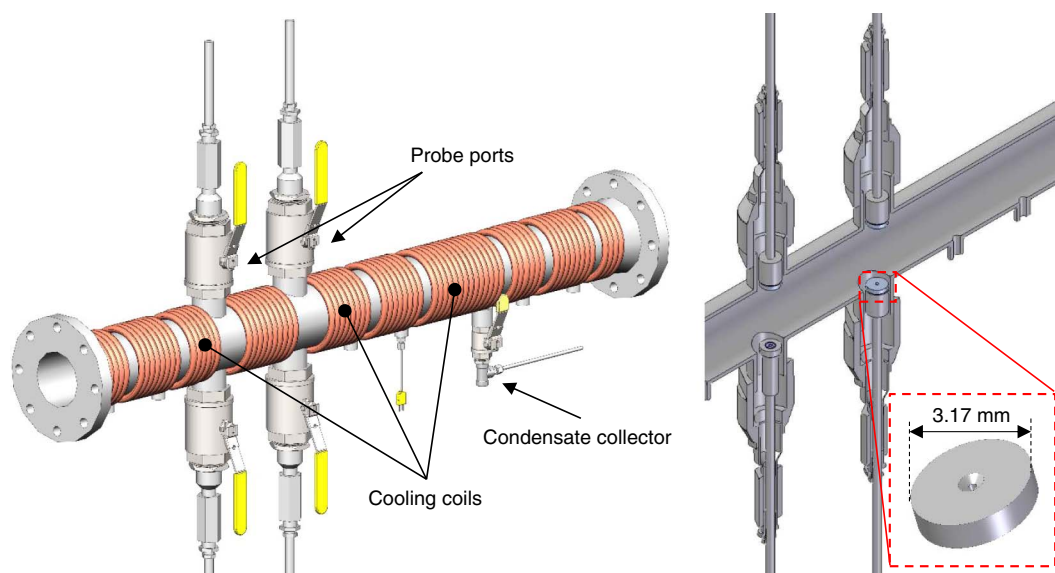


FIGURE 9. Schematic of the test section in high-pressure high-temperature corrosion flow loop (left view); cross section of the corrosion probe with its mounted corrosion sample (right view).

concept of droplet transport as an effective TLC mitigation method. A corrosion inhibitor was injected in the bulk liquid phase under stratified flow conditions, with or without droplet entrainment present in the gas phase. TLC rates were measured on steel specimens installed in a custom designed cooled TLC test section.

Experimental Procedure

The experimental corrosion study was performed on the same large scale flow loop used for the determination of droplet entrainment, with the test section modified to suit high-pressure and high-temperature conditions. The flow loop was equipped with two identical test sections, designed to investigate TLC. The test sections were 4 in (0.102 m) inner diameter (ID) pipe made of UNS S31600 and equipped with eight 2 in (0.051 m) ID probe ports through which corrosion measurements devices could be inserted (Figure 9, left hand side). Four of these ports were located at the bottom of the pipe (6 o'clock position), while the other four ports were located at the top of the pipe (12 o'clock position). Copper coils were wrapped around the pipe and used to circulate cooling water. The water condensation rate was measured using a condensed water collector located downstream of the test section. The gas and inner pipe wall temperatures were measured continuously during the experiments. A more detailed description of the experimental setup can be found elsewhere.¹

For each test, the liquid phase consisted of an aqueous solution containing 1 wt% sodium chloride (NaCl), deoxygenated with CO₂ prior to the tests (O₂ concentration around 20 ppb). The pH of the solution

was set constant to 5.9 and controlled by addition of sodium hydroxide to decrease the aggressiveness of the environment and enhance the corrosion inhibitor efficiency. The gas phase consisted of a CO₂/SF₆ mixture with 70 mol% SF₆; the equivalent methane pressure was 2.85 MPa. The liquid phase in the tank was heated to the required temperature using immersion heaters. The gas blower and the liquid pump were used to get the desired gas and liquid flow rates, respectively.

The corrosion samples used in experiments were carbon steel (CS) UNS K03014 with a 7.2 cm² exposed area to the corrosive fluid (Figure 9, right hand side). The chemical composition of the steel is detailed in Table 5; its analysis revealed a quenched and tempered microstructure (Figure 10) after polishing with a diamond suspension and etching with a Nital solution (5 vol% nitric acid, 95 vol% ethanol).²⁵ CS specimens were polished with 220, 400, and 600 grit silicon carbide paper under a flush of isopropanol before any testing. During the experiment, two samples at the bottom and three at the top of the pipe were flush mounted in the test section.

The corrosion inhibitor was selected based on its past demonstrated efficiency against bottom of the

TABLE 5
Chemical Composition of the Carbon Steel
UNS K03014 (wt%) (Balance Fe)

Al	As	C	Co	Cr	Cu	Mn	Mo	Nb
0.0033	0.015	0.140	0.012	0.150	0.140	1.180	0.160	0.027
Ni	P	S	Sb	Si	Sn	Ti	V	Zr
0.380	0.012	0.003	0.035	0.250	0.012	0.002	0.052	0.004

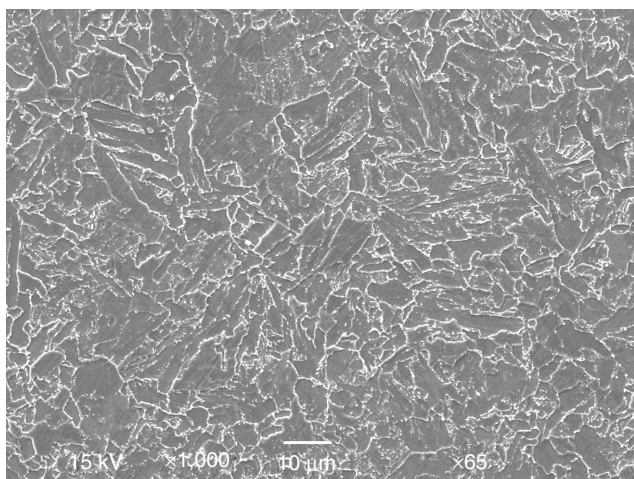


FIGURE 10. SEM image of the carbon steel sample surface quenched and tempered (etched with 5% Nital).

line corrosion (BLC)²⁶⁻²⁷ and consisted of a 24% tall oil fatty acid (TOFA)/Diethylene triamine (DETA) imidazoline. A non-volatile inhibitor was preferred in this study because a mechanical mass transfer by droplet entrainment was the only intended way of transporting the inhibitor to the top of the pipe.

Three independent tests (A, B, and C) were conducted using different superficial gas velocities and inhibitor concentrations to measure both BLC and TLC. In test A, the superficial liquid and gas velocities were selected to ensure a stratified flow regime, while limiting any significant droplet entrainment in the pipe. The liquid droplets eventually present at the top of the pipe would only result from the condensation of water vapor due to the cooling of the pipe wall. In tests B and C, an increase in superficial gas velocity from 3.2 m/s to 6.9 m/s changed the flow regime from stratified without droplet entrainment to stratified with droplet entrainment and deposition at the top of the pipe. In test C, 300 ppm of corrosion inhibitor was injected to evaluate the inhibition effect on both BLC and TLC. Details about the operating conditions used during those tests are given in Table 6.

Experimental Results

Corrosion Rate Analysis — Corrosion rates in this experimental study were measured using the weight loss method on the samples located at both bottom and top of the line for tests A, B, and C (Figure 11). At the bottom of the pipe, the baseline test (A) exhibited a high corrosion rate of 8.4 mm/y because of the combination of high-temperature conditions and the absence of corrosion inhibitor (Figure 11). The gas flow rate was doubled from test A to test B and, consequently, the corrosion rate increased to a higher value of 11.7 mm/y. The higher superficial gas velocity increased the in situ aqueous velocity (from 0.58 m/s to 1.23 m/s) as a result of slippage, which, in turn,

TABLE 6

Test Conditions for TLC Experiments

Parameters	Conditions		
Gas temperature (°C)	70 to 72		
Gas composition (mol%)	70.2 (SF ₆) + CO ₂ (29.8)		
Equivalent CH ₄ pressure (MPa)	2.85		
NaCl solution (wt%)	1		
Solution pH (-)	5.9		
Test duration (day)	2		
	Test A	Test B	Test C
Superficial liquid velocity (m/s)	0.06	0.06	0.06
Superficial gas velocity (m/s)	3.2	6.9	6.9
Inhibitor concentration (ppm)	0	0	300
Flow pattern	SW	SW	SW
Droplet entrainment in pipe	no	YES	YES
In situ liquid velocity (m/s)	0.58	1.23	1.23
Predicted water condensation rate (mL/m ² /s)	0.14	0.25	0.25
Predicted droplet deposition rate (mL/m ² /s)	0	2.16	2.16

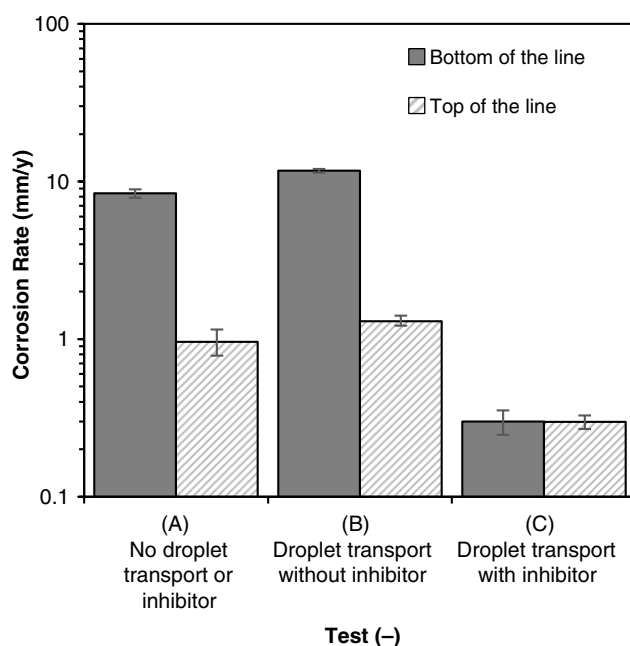


FIGURE 11. BLC and TLC rates in absence/presence of droplet transport and corrosion inhibitor.

enhanced the transport of corrosive species to the steel surface. Under the same operating conditions, the corrosiveness of the medium was mitigated by the addition of 300 ppm of inhibitor (test C); the BLC rate drastically dropped to 0.3 mm/y, which represents an inhibition efficiency of 97.4%.

The measured TLC rates show the same trend as the measured BLC rates (Figure 11). The baseline test (A) exhibited a TLC rate of 0.96 mm/y resulting from the sole presence of condensed water at the top of the pipe. More corrosive conditions were experienced at higher gas velocity with significant droplet transport, yielding a corrosion rate of 1.3 mm/y (test B). A higher

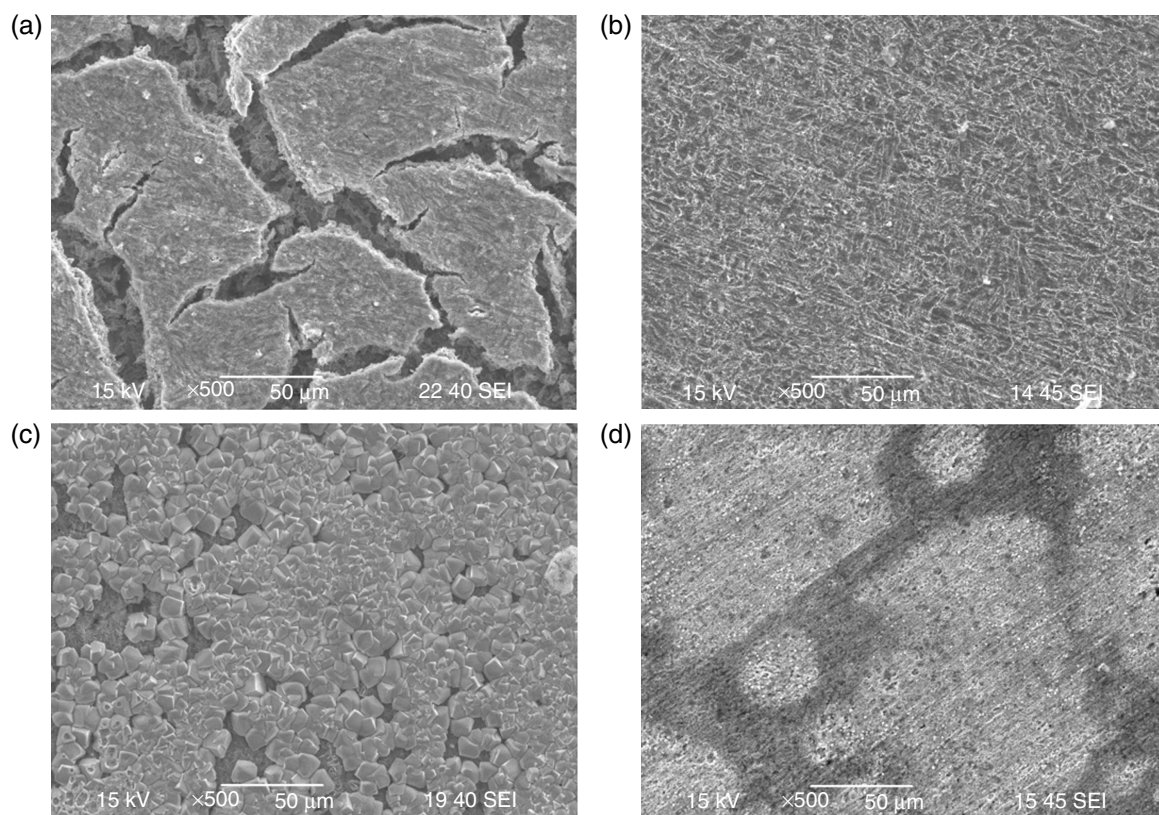


FIGURE 12. SEM images of sample surfaces in an inhibitor-free environment (test B): (a) BLC and (b) TLC; and in environment with 300 ppm inhibitor (test C): (c) BLC and (d) TLC.

superficial gas velocity promoted not only the entrainment and deposition of water droplets at the top of the pipe ($2.16 \text{ mL/m}^2/\text{s}$), but also enhanced the heat transfer at the pipe wall leading to higher water condensation rates ($0.25 \text{ mL/m}^2/\text{s}$). The injection of 300 ppm of corrosion inhibitor in test C mitigated the CO_2 corrosion attack at the top of the line with a TLC rate dropping to 0.3 mm/y , which is the same as the inhibited BLC rate, as the inhibitor concentration at the top and bottom of the line was similar. In the absence of a volatile corrosion inhibitor, the inhibition was only possible by utilizing the mechanical entrainment of liquid droplets to transport the chemical inhibitor to the top of the pipe. This method can only be effective to mitigate TLC as long as the droplet deposition rate remains higher than the water condensation rate as it was demonstrated in the present test. In field conditions, the water phase only represents a small volume fraction of the liquids eventually present in the gas pipeline. As non-volatile corrosion inhibitors are usually not soluble in the hydrocarbon phase, the use of oil dispersible inhibitors may be warranted in field conditions.

Surface Analysis — A scanning electron microscope (SEM) surface analysis of the steel samples exposed to BLC and TLC conditions was conducted after tests B and C (Figure 12). In the absence of

corrosion inhibitor, the BLC specimen showed a “cracked” iron carbide (Fe_3C) layer typically observed in CO_2 corrosion (Figure 12[a]). In the presence of corrosion inhibitor, the BLC specimen still had signs of the polishing marks, signifying a less aggressive corrosion medium (Figure 12[b]). Crystals of iron carbonate (FeCO_3) were observed on the TLC specimen in an inhibitor-free environment (Figure 12[c]). No FeCO_3 was observed on the TLC specimen surface (Figure 12[d]), which confirms the effective transport of corrosion inhibitor to the top of the pipe by a mechanism of droplet entrainment/deposition.

CONCLUSIONS

❖ This study investigated the entrainment and deposition of liquid droplets in a gas phase as a potential solution to transport a non-volatile corrosion inhibitor to the top of the pipe. A mechanistic model was developed to predict the onset of droplet entrainment in horizontal and near-horizontal pipes under gas-liquid two-phase conditions. The model was further validated using newly acquired data from a large scale flow loop mimicking operating conditions similar to those encountered in wet gas transportation lines.

❖ Using controlled multiphase flow and water condensation conditions, corrosion experimentation in a high-pressure high-temperature large scale flow loop additionally demonstrated that CO₂ top of line corrosion could be mitigated by transporting a non-volatile corrosion inhibitor to the top by droplet entrainment.

ACKNOWLEDGMENTS

The authors would like to acknowledge the sponsors of the Top of the Line Corrosion JIP and the technical support from the Institute for Corrosion and Multiphase Technology (ICMT) at Ohio University. The authors wish to extend their appreciation to Cody Shafer for the 3D technical drawings of the TLC flow loop.

REFERENCES

- M. Singer, D. Hinkson, Z. Zhang, H. Wang, S. Nešić, *Corrosion* 69, 7 (2013): p. 719-735.
- Y. Gunaltun, D. Larrey, *Oil Gas J.* 98, 28 (2000): p. 58-63.
- Y. Gunaltun, D. Supriyatman, J. Achmad, *Oil Gas J.* 28, 1 (1999): p. 64-71.
- Y. Gunaltun, D. Larrey, *Oil Gas J.* 98, 29 (2000): p. 68-71.
- U. Kaewpradap, M. Singer, S. Nešić, S. Punpruk, *Corrosion* 73, 8 (2017): p. 1007-1016.
- Y. Gunaltun, "Design of Multiphase Offshore Pipelines with High Risk of Sweet Top of the Line Corrosion," CORROSION 2013, paper no. 2290 (Houston, TX: NACE International, 2013).
- Z. Belarbi, F. Farelas, M. Singer, S. Nešić, *Corrosion* 72, 10 (2016): p. 1300-1310.
- Z. Belarbi, T.N. Vu, F. Farelas, M. Singer, S. Nešić, *Corrosion* 73, 7 (2017): p. 892-899.
- Y. Gunaltun, T.E. Pou, M. Singer, C. Duret, S. Espitalier, "Laboratory Testing of Volatile Corrosion Inhibitors," CORROSION 2010, paper no. 10095 (Houston, TX: NACE, 2010).
- Z. Zhang, "A Study of Top of the Line Corrosion Under Dropwise Condensation" (Ph.D. diss., Ohio University, 2008), p. 204.
- M. Singer, "Top-of-the-Line Corrosion," in *Trends in Oil and Gas Corrosion Research and Technologies. Production and Transmission*, ed. A.M. El-Sherik, 1st ed. (Amsterdam, Netherlands: Woodhead Publishing, 2017), p. 385-408.
- D. Tayebi, S. Nuland, P. Fuchs, *Int. J. Multiphase Flow* 26, 5 (2000): p. 741-761.
- H. Han, K.S. Gabriel, *J. Fluids Eng. Trans. ASME* 129, 3 (2007): p. 293-301.
- M. Ishii, M.A. Grolmes, *AIChE J.* 21, 2 (1975): p. 308-318.
- I. Kataoka, M. Ishii, K. Mishima, *J. Fluids Eng. Trans. ASME* 105, 2 (1983): p. 230-238.
- D.E. Woodmansee, T.J. Hanratty, *Chem. Eng. Sci.* 24, 2 (1969): p. 299-307.
- J.J. Van Rossum, *Chem. Eng. Sci.* 11, 1 (1959): p. 35-52.
- G.F. Hewitt, N.S. Hall-Taylor, *Annular Two-Phase Flow*, 1st ed. (Oxford, United Kingdom: Pergamon Press, 1970), p. 141-147.
- I. Mantilla, L.E. Gomez, R.S. Mohan, O. Shoham, G.E. Kouba, R. Roberts, "Modeling of Liquid Entrainment in Gas in Horizontal Pipes," ASME Fluids Engineering Division Summer Conference, paper no. FEDSM2009-78459 (New York, NY: American Society of Mechanical Engineers, 2009).
- G.A. Hughmark, *AIChE J.* 19, 5 (1973): p. 1062-1065.
- N. Jauseau, "Multiphase Flow Effects on Naphthenic Acid Corrosion of Carbon Steel" (Ph.D. diss., Ohio University, 2012), p. 187.
- A. Al-Sarkhi, C. Sarica, K.L. Magrini, *AIChE J.* 58, 4 (2012): p. 1018-1029.
- N. Andritsos, "Effect of Pipe Diameter and Liquid Viscosity on Horizontal Stratified Flow" (Ph.D. diss., University of Illinois, 1986).
- I. Mantilla, "Mechanistic Modeling of Liquid Entrainment in Gas in Horizontal Pipes" (Ph.D. diss., University of Tulsa, 2008), p. 59.
- ASTM E407-07, "Standard Practice for Microetching Metals and Alloys" (West Conshohocken, PA: ASTM International, 2007).
- I. Jevremovic, M. Singer, S. Nešić, V. Miskovic Stankovic, *Mater. Corros.* 67, 7 (2015): p. 756-768.
- I. Jevremovic, M. Singer, S. Nešić, V. Miskovic-Stankovic, *Corros. Sci.* 77 (2013): p. 265-272.

NOMENCLATURE

Latin Symbols

c	wave celerity (m/s)
CR	corrosion rate (mm/y)
D	diameter (m)
e _R	relative error (-)
F	force (N)
f	fanning friction factor (-)
g	gravity constant (g = 9.81 m/s ²)
h	height (m)
L	length (m)
MW	molecular weight (g/mol)
P	pressure (bara)
T	temperature (°C)
U	velocity (m/s)
X*	Froude number ratio (-)

Greek Symbols

β	pipe inclination angle (degree)
ε ₁	average relative error (%)
ε ₂	absolute average relative error (%)
ε ₃	standard deviation of relative error (%)
λ	length (m)
μ	dynamic viscosity (kg/m/s)
ρ	density (kg/m ³)
σ	surface tension (N/m)
τ	shear stress (Pa)

Superscripts

0	standard conditions (101.3 kPa, 15.6°C)
---	---

Subscripts

crit	relating to entrainment onset conditions
D	relating to the drag force
exp	relating to experimental measurements
G	based on the gas phase
g	relating to the gravity force
i	relating to the gas/liquid interface
L	based on the liquid phase
pred	relating to predicted values
S	relating to the interfacial shape
SG	based on the superficial gas
SL	based on the superficial liquid
w	relating to the wave
σ	relating to the surface tension force

Dimensionless Numbers

Fr	Froude number
N _μ	viscosity number
Re	Reynolds number

APPENDIX A: ENTRAINMENT ONSET VELOCITY DATA

Parameters	Operating Conditions and Measurements												
	0	0	0	0	0	0.339	0.506	0.606	0.672	0.719	0.719	0.719	0.719
SF ₆ mol fraction in gas phase	0	0	0	0	0	0.339	0.506	0.606	0.672	0.719	0.719	0.719	0.719
Gas density (kg/m ³) ^(A)	3.1	4.3	5.5	6.6	7.9	6.5	10.6	14.9	19.1	9.7	13.2	16.6	23.6
Gas viscosity (10 ⁶ × Pa·s) ^(B)	15.2	15.1	15.2	15.4	15.5	15.9	16.3	16.4	16.6	16.7	16.6	16.7	16.6
Operating pressure (MPa)	0.172	0.238	0.307	0.375	0.446	0.203	0.273	0.344	0.413	0.207	0.276	0.346	0.482
Equivalent pressure CH ₄ (MPa)	0.470	0.652	0.841	1.028	1.225	0.991	1.625	2.265	2.898	1.508	2.021	2.530	3.533
Operating temperature (°C)	27.43	25.72	27.62	32.27	32.85	26.83	29.52	29.04	30.84	31.88	29.86	31.29	29.23
U _{SL} (m/s)	U _{SG} (m/s)												
0.004	N/A	N/A	10.62	10.87	11.41	N/A	9.11	9.36	N/A	8.99	9.73	N/A	N/A
0.007	10.47	10.43	9.65	9.62	9.45	9.10	8.29	8.34	N/A	8.34	7.97	7.83	N/A
0.011	10.49	9.75	9.53	8.96	9.03	8.86	8.04	7.89	N/A	8.34	8.11	7.56	N/A
0.014	10.16	9.61	9.29	8.78	8.95	9.00	8.03	8.00	7.20	8.05	8.09	7.58	6.49
0.018	9.99	9.63	9.30	8.61	8.97	8.71	7.89	7.96	7.14	7.89	7.95	7.10	6.50
0.022	9.98	9.37	8.98	8.43	8.79	8.69	7.91	7.65	7.18	7.87	7.88	7.12	6.49
0.025	9.97	9.27	8.96	8.42	8.58	8.50	7.71	7.67	7.16	7.77	7.78	7.09	6.32
0.029	9.64	9.15	8.99	8.61	8.23	8.34	7.71	7.56	6.84	7.81	7.70	7.11	6.66
0.032	9.72	8.95	8.59	8.43	8.20	8.01	7.69	7.69	6.66	7.83	7.82	6.81	6.34
0.036	9.58	9.09	8.58	8.40	8.18	7.87	7.54	7.51	6.62	7.73	7.50	6.97	6.29
0.04	9.45	8.95	8.53	8.38	8.03	7.86	7.20	7.50	6.51	7.46	7.63	7.09	6.33
0.043	9.79	8.93	8.26	8.01	8.18	7.83	7.37	7.46	6.63	7.36	7.32	6.97	6.31
0.047	9.75	8.57	8.36	8.02	7.93	7.60	7.18	7.38	6.51	7.33	7.31	6.84	6.33
0.05	9.45	8.88	8.25	8.03	7.76	7.88	6.97	7.35	6.62	7.58	7.04	6.99	6.32
0.054	8.93	8.71	8.28	7.91	7.76	7.66	7.31	7.37	7.02	7.24	7.15	6.76	6.29
0.058	9.08	8.49	7.84	7.93	7.86	7.50	6.94	7.18	6.50	7.32	7.29	6.75	6.29
0.061	8.90	8.24	7.97	8.12	7.92	7.63	6.93	7.19	6.53	7.31	7.28	6.41	6.29
0.065	8.59	8.34	7.99	7.74	7.58	7.40	6.98	6.79	6.48	7.29	6.89	6.74	6.24
0.068	8.60	8.26	8.21	7.96	7.47	7.71	6.89	6.61	6.88	6.99	6.96	6.22	5.92
0.072	8.73	8.21	7.56	7.57	7.44	7.79	7.01	6.40	6.45	6.86	6.71	6.25	5.88

^(A) The gas density was computed with the PVT simulator Multiflash™ (version 6.1).

^(B) The gas viscosity was computed with the PVT simulator Multiflash™ (version 6.1).